Supplementary Information

# Tissue Fluidity Promotes Epithelial Wound Healing

Robert J. Tetley, Michael F. Staddon, Davide Heller, Andreas Hoppe, Shiladitya Banerjee, Yanlan Mao

Contents

## Methods

### *Drosophila* strains

*Drosophila* stocks were raised on conventional cornmeal media at 25˚C. The following alleles and transgenes were used experimentally: *shg*-GFP[1] (II, referred to as Ecad-GFP), *sqh*-mCherry[2] (III), *rn*-GAL4 (III, MiMIC insertion), UAS-R*ok*-RNAi (II, VDRC KK Library), UAS-*Mbs*-RNAi (II, VDRC KK Library), *sqh*-GFP[3] (II), *shg*-tdTomato[1] (II, referred to as Ecad-tdTomato), *sqh*$^{AX3}$ (X)[4], ubi-*shg*-GFP (II, referred to as ubi-Ecad-GFP)[5]. The experimental genotypes used and their corresponding data are shown in Table 1.

| Genotype | Corresponding Figures and Videos |
|---|---|
| *sqh*$^{AX3}$; *sqh*-GFP, Ecad-tdTomato | Fig. 1a, c, Fig. 3a, Supplementary Video 1 |
| *yw*; Ecad-GFP/+; *rn*-GAL4/+ (referred to as WT) | Fig. 1b, e-g, Fig. 3b-g, i, Fig. 5b, e-g, Supplementary Fig. 1a-d, Supplementary Fig. 3a, Supplementary Fig. 4e, Supplementary Fig. 6a-d, Supplementary Figure 9b-c, Supplementary Video 2, Supplementary Video 5 |
| Ecad-GFP; *sqh*-mCherry, *pnr*-GAL4 | Fig. 1d |
| *yw*; Ecad-tdTomato | Fig. 3h-i |
| *yw*; Ecad-GFP/UAS-*Mbs*-RNAi; *rn*-GAL4/+ (referred to as *Mbs*-RNAi) | Fig. 5b-c, e-g, Supplementary Fig. 4e, Supplementary Fig. 6a-d, Supplementary Fig. 7a-e, Supplementary Fig. 9b-c, Supplementary Video 6 |
| *yw*; Ecad-GFP/UAS-R*ok*-RNAi; *rn*-GAL4/+ (referred to as *Rok*-RNAi) | Fig. 5b, d-g, Supplementary Fig. 4e, Supplementary Fig. 6a-d, Supplementary Fig. 8a-e, Supplementary Fig. 9b-c, Supplementary Video 7 |
| *w*; ubi-Ecad-GFP | Supplementary Fig. 6a-d, Supplementary Fig. 9a-h |

**Table 1. *Drosophila* experimental genotypes and corresponding data**

### Live imaging of wing imaginal discs

Late third instar wing imaginal discs were cultured in Shields and Sang M3 media (Sigma) supplemented with 2% FBS (Sigma), 1% pen/strep (Gibco), 3ng/ml ecdysone (Sigma) and 2ng/ml insulin (Sigma). Wing discs were cultured in 35mm fluorodishes (WPI) under 12mm filters (Millicell), as described elsewhere[6]. Wing discs were imaged on a Zeiss LSM 880 microscope with Airyscan at 512x512 resolution with a 63x objective (NA 1.4) at 5x zoom. Laser power of 0.2-0.3% was used and images were captured with a 0.5µm z-spacing. Time intervals varied depending on the experiment. For single channel wounding experiments, the first 25 images were captured with no time interval (to visualise the fast, early dynamics of

wound closure, using a sufficient z-stack depth to include all cells in the field of view). For two channel wounding experiments, the first 12 images were captured with no time interval. Subsequent imaging was then performed with a time interval of 3 minutes for both single and two channel experiments, with a total z-stack depth of approximately 40 μm, until wounds closed. For experiments measuring unwounded intercalation rates, a time interval of 3 minutes was used for a total imaging time of 2 hours.

**Wounding of tissues**

Wing discs were wounded using a pulsed Chameleon Vision II TiSa laser (Coherent), tuned to 760nm. Ablation was performed on small, manually defined circular regions of interest (ROIs) that coincided with the tricellular junctions shared between all cells to be ablated. This was necessary, as larger ROIs produced significant autofluorescent scarring that made subsequent image analysis impossible. Furthermore, ablation of larger regions led to cavitation, which masked the initial recoil dynamics of the wound. Ablation was performed in a single z-plane, at the level of the adherens junctions.

**Segmentation and tracking of wound time-lapse images**

Ecad time-lapse images were first deconvolved using Huygens (Scientific Volume Imaging). Deconvolved images were segmented, tracked and analysed using EpiTools[7]. The following MATLAB-based analysis modules were implemented in the following order: Adaptive projection, Contrast Enhancement (CLAHE), Cell segmentation, Automatic seed tracking, Re-segmentation, Generate skeletons. The adaptive projection method originally developed for EpiTools[7] was extended through an additional plugin that allowed the user to interactively control and guide the automated creation of the projection surface. This was necessary in regions with strong peripodial membrane signal just above the main layer of cells or in regions with strong surface gradients which could lead to a misaligned surface. The interactive tool suggested surface markers at locations with sufficient cell signal intensity in the 3D image volume. Additional markers could be added or removed by the user. The markers were used to guide the surface fitting procedure in EpiTools[7] by providing a first estimate of the projection surface location which would be refined in a second iteration of the surface fitting using the cell signal intensities in its local vicinity. Cell signal intensities along the fitted surface within the 3D image volume formed the final projection image. The settings used for “Adapative projection” and “Cell segmentation” were selected on a case-by-case basis, to give the best result for each time-lapse image. Default settings were used for “Contrast Enhancement (CLAHE). “Automatic seed tracking” was implemented so that each cell had a single seed, where possible. Corrected seeds were used for “Re-segmentation” and the resulting corrected segmentation was used to “Generate skeletons”. The remaining segmentation and tracking was performed using EpiTools’ Icy Plugins. Skeletons were manually corrected using “CellEditor”. The corrected skeletons were used to implement “CellGraph”, which was run using the “STABLE_MARRIAGE” algorithm for tracking with a Propagation Limit of 5 frames without cutting any border lines. To allow manual tracking correction, an additional helper tool was developed as part of the EpiTools[7] plugins for icy (code and executable of this customized version of the plugins for Icy are publicly available at: *github.com/epitools/manual_tracking*). The correction functionality is accessible through the TEST tool in the CellOverlay icy plugin. The new user interface guides the user in the correction process by

visualizing a superimposition of two consecutive time points (frames). This feature is implemented by displaying the segmentation skeleton of the previous frame (t - 1) on top of the current frame (t) and highlighting the cell to be linked in the skeleton. The user can link the highlighted cell by clicking on any cell in the current frame (t). Optionally the user can also choose to connect the current cell track to another existing track (i.e. merge the two tracks into one) or register a cell division or cell elimination event. The underlying procedure saves any tracking correction to an external file as backup and merges modifications with existing tracking information, from EpiTools itself or other sources.

**Quantitative analysis of wound time-lapse images**

The following data was quantified and exported using the "CellOverlay" Icy plugin in EpiTools[7]. Statistical analysis and curve fitting was performed in Prism (GraphPad):

*Wound area* – the killed cells and resulting wound were manually selected using the "CELL_COLOR_TAG" tool and data exported. Wound area was then expressed as a percentage of the total area of all the killed cells.

*Wound edge junctions remaining* – the initial number of wound edge cells was counted manually prior to wounding. The polygon number of the wound was quantified using the "CELL_COLOR_TAG" tool. The wound polygon number was expressed as a percentage of the initial number of wound edge cells. When percentage of junctions remaining data was pooled from multiple wing discs a moving average curve (±4 time points) was fitted to the data.

*Distinction of fast and slow closure phases* – a two-phase exponential decay curve was fitted to the cell area data pooled from multiple wing discs. The fast and slow phases of closure are represented by the ranges of the fast and slow exponential decays respectively.

*Intercalation rates* – an intercalation was defined as the loss of a cell-cell junction that was subsequently replaced by a new junction in the orthogonal direction. When quantifying such events, two rules were introduced: 1) to buffer against segmentation errors that lead to the false identification of an intercalation, only intercalations in which the new junction persisted for at least 6 minutes were scored, 2) as junctions were roughly 12 pixels in width, the segmentation software was unable to accurately recognise very short junctions or transient 4-way vertices. Therefore, any junction under 6 pixels in length was assigned a length of 0, meaning that cells were considered to be in a 4-way vertex configuration. To extract intercalation data, the "EDGE_T1_TRANSITIONS" tool was run and data exported. To enable the tracking of T1 transitions at a better granularity, the edge tracking framework in EpiTools[7] was rewritten to make it possible to track edges from a frame of choice. Several output statistics were added to the data export, including a summary report for the number of edges and t1 transitions in each frame. The visualization of the "EDGE_T1_TRANSITIONS" tool was also improved by labelling individual edges with respect to their tracking status. The code and executable for all the discussed modifications is included in the customized version linked above. To quantify intercalations in the tissue (rather than at the wound edge), "EDGE_T1_TRANSITIONS" was initialised in the first time point. To quantify intercalations at the wound edge, "EDGE_T1_TRANSITIONS" was initialised in the

second time point, after the wound had been generated. The wound itself was treated as a cell, meaning an intercalating tetrad was formed of three wound edge cells and the wound. Intercalation analysis was performed only on junctions that were present in the time point at which "EDGE_T1_TRANSITIONS" was initialised. Junction loss events were scored in the time point immediately prior to the formation of a stable new junction. At each time point, the number of junctions lost was expressed as a percentage of the total number of junctions. These values were then summed and divided by the total time (in hours) to obtain an intercalation rate expressed as Percentage of Junctions Lost/hour.

*Cell Division Rates* - the number of cells dividing was exported from the "DIVISIONS_AND_ELIMINATIONS" tool and expressed as a percentage of the total number of cells obtained from the "TRACKING_STABLE_ONLY" tool. This was then divided by the total time of each movie to give Percentage of Cells Dividing/hour.

*Polygon distributions of wound edge cells* – initial wound edge cells were selected manually using the "CELL_COLOR_TAG" tool, prior to wounding. These identities were propagated through all time points. Data was exported and the polygon distributions quantified by pooling all data from all wound edge cells in all wing discs. Polygon distributions were quantified at time points prior to and immediately after wounding and immediately after closure.

*Cell elongation* – cell elongation was calculated by dividing the major and minor axis length of best fit ellipses (exported from the "CELL_COLOR_TAG" tool). The mean elongation of pooled cells was calculated prior to wounding. Changes in mean cell elongation were expressed as a percentage of the initial mean elongation.

Overlay images were generated by selecting the relevant "CellOverlay" tool layer.

**Myosin II quantification**

Myosin II was quantified during the first hour post wounding of $sqh^{AX3}$; *sqh*-GFP, Ecad-tdTomato wing discs, using Sqh-GFP as a reporter. Because these experiments were performed in a $sqh^{AX3}$ null background, all molecules of Myosin II were tagged with GFP. First, raw (not deconvolved) Sqh-GFP images were background subtracted using the Rolling Ball tool in FIJI with a radius of 12 pixels. Maximum intensity projections (MIPs) of Sqh-GFP images were then generated, which excluded any signal from the overlying peripodial membrane cells. The CellGraph function of EpiTools was run on the Sqh-GFP MIPs using the segmented skeleton images from the corresponding deconvolved Ecad-tdTomato channel (segmentation performed as above).

Junctions were selected manually using the "EDGE_COLOR_TAG" CellOverlay tool in EpiTools[7]. Edge Intensity Buffer and Vertex Intensity Buffer were set to 3 and Selection Mode 1 was used to exclude vertices from the quantification. Two groups of junctions were selected in each movie; 1) junctions in contact with the wound edge in each frame and 2) 10 junctions in the surrounding tissue that persisted for the entire time window of quantification, were more than one cell diameter away from the wound and were not associated with a cell division event. Mean Sqh-GFP intensities were exported for all tagged junctions, with the mean calculated from the top 90% of pixel intensities for each junction (to exclude any dark pixels that were outside of the cell's cortex). Wound edge junction intensities were

normalised to the mean intensity of the 10 junctions in the surrounding tissue for each time point. The relative normalised intensity of wound edge junctions was then calculated by dividing by the mean normalised intensity of wound edge junctions in the time point prior to wounding (t0).

**Assigning cell row fates (Fig. 3c-e)**
Cells were assigned row identities using the "CELL_COLOR_TAG" CellOverlay tool in EpiTools[7]. This was done prior to wounding and these identities were propagated in time through the entire movie. Cells could therefore change rows over time (by intercalation), but still retained their initially assigned identities (Supplementary Video 5).

**Intercalation row analysis (Fig. 3g)**
An intercalation co-ordinate was calculated for every intercalation event (tissue and wound edge) as the intersect between the centroids of the four intercalating cells or three intercalating cells and the wound, at the time point immediately prior to the formation of a new stable junction. To simplify analysis, the wound was considered as a circle of the same area quantified for the wound at a given time point, giving a standardised wound radius ($wound^{radius}$). Rows of cells were considered as concentric rings around the central wound, the diameter of each row ($row^{diameter}$) being the mean diameter of cells for a particular movie. Row identities were assigned at each time point, rather than being initialised in the first time point, meaning that cells could change row identities over time (for instance, a row 1 cell could become a row 2 cell after intercalating away from the wound edge). The distance between the wound centroid and intercalation co-ordinate ($Ical^{distance}$) was calculated for every intercalation event. To determine which row away from the wound the intercalation fell into, the following calculation was used:

$$(Ical^{distance} - wound^{radius})/row^{diameter}$$

The value obtained was then rounded up to the nearest integer, which referred to the row number. The number of intercalations in a row, at a particular time point, was scored and divided by the area of the row (which changed over time as the area of the wound reduced). These values were summed and divided by the total time of the movie (in hours) to give an intercalation rate in Intercalations/$\mu m^2$/hour.

**Vertex model**
We model the apical surface of the tissue as a 2D network of polygonal cells, with cell-cell interfaces represented by straight edges, and three-way junctions by vertices. The total mechanical energy of the tissue is given by[8]:

$$E = \sum_{\alpha} \frac{1}{2} K (A_\alpha - A_\alpha^0)^2 + \sum_{\alpha} \frac{1}{2} \Gamma P_\alpha^2 + \sum_{\langle i,j \rangle} \Lambda_{ij} l_{ij}$$

where the individual cells are labelled by $\alpha$, and the edges connecting vertices $i$ and $j$ by $\langle i, j \rangle$ (Supplementary Fig. 2). The first term represents the area elasticity of the cells, with elastic modulus $K$, $A_\alpha$ is the area of cell $\alpha$ and $A_\alpha^0$ is the preferred area. The second term represents contractile energy of the actomyosin cortex for a cell with perimeter $P_\alpha$, and contractile tension, $\Gamma$. The final term represents the energy cost due to line tensions $\Lambda_{ij}$ acting on edges of length $l_{ij}$ which is a combination of

cell-cell adhesion and cortical tension. Negative line tension implies cell-cell adhesion dominates over cortical tension, such that cells tend to maximize the length of junctions between their neighbors. The net mechanical force acting on the vertex $i$ is given by $\boldsymbol{F}_i = -\partial E/\partial \boldsymbol{x}_i$. Assuming over-damped dynamics, the equation of motion for vertex $i$ is:

$$\mu \frac{d\boldsymbol{x}_i}{dt} = \boldsymbol{F}_i$$

where $\mu$ is the coefficient of friction.

In this study, we non-dimensionalize energy by $K/A_0^2$ and length by $A_0^{1/2}$, resulting in normalized contractility $\bar{\Gamma} = \Gamma/KA_0$ and normalized line tension $\bar{\Lambda} = \Lambda/KA_0^{3/2}$. Time is non-dimensionalized by the $T^* = \mu/KA_0$. The equation of motion is discretized as:

$\bar{\boldsymbol{x}}_i(t+\Delta t) = \bar{\boldsymbol{x}}_i(t) + \frac{\Delta t}{T^*}\bar{\boldsymbol{F}}_i$,

where $\Delta t$ is the timestep. See Table 2 for a complete list of default parameter values. As the tissue relaxes by minimizing mechanical energy, cell edges may shrink due to contractile forces. If an edge length goes below a small threshold length, $L_{T1}$, an intercalation, or T1 transition, occurs, in which a new edge is formed perpendicular to the original junction, if it results in a lower energy. To keep the system out of equilibrium, we introduce two sources of activity: cell division, and line tension fluctuations, as described below.

*Cell division* - we implemented a simplified model of the cell cycle, with cells in one of three phases; resting, growing or dividing. Cells start in the resting phase, with the default preferred area $A_0$. Once they have reached a threshold age, they transition to mitosis at a fixed rate. In mitosis, the preferred area of the cell doubles over a period of 30 minutes, resulting in growth of the cell. After 30 minutes, the cell is divided into two new cells by creating a new edge between two of the cell edges which is chosen to minimize the system energy. This results in division of elongated cells along their short axis.

*Line tension fluctuations* **-** to model myosin II fluctuations, we allow the line tensions to fluctuate over time, adapting the model introduced in Curran ***et al.***[9] .The line tension $\Lambda_{ij}$ on the edge joining vertices $i$ and $j$ evolves over time as:

$$\frac{d\bar{\Lambda}_{ij}}{dt}(t) = -\frac{1}{\tau_m}\left(\bar{\Lambda}_{ij}(t) - \bar{\Lambda}_0\right) + \xi_{ij}(t)$$

where $\tau_m$is a persistence time of myosin, $\bar{\Lambda}_0$ is the mean line tension, and $\xi_{ij}$ is an uncorrelated white noise obeying:

$\langle \xi_{ij}(t)\xi_{kl}(t')\rangle = \frac{2\sigma_m^2}{\tau_m}\delta(t-t')\delta_{ik}\delta_{jl}$.

The line tension deviation, $\sigma_m$, controls the amount of fluctuation around the mean, and is equal to the standard deviation of the line tension over time.

**Modelling laser ablation and wound healing**

Wounds in the epithelium are created by removing any cell that lies partially or fully within a circle of radius $R_w$. As material remains within the wound, but the actomyosin cortices are disrupted, we remove all contractility within the wound. The polygons constituting the wound have an area elasticity term with elastic modulus $K_w$ and zero contractility. As tissue material leaves the gap during wound closure, the elastic modulus decreases to zero over 10 minutes. At the same time, tension in the

purse-string surrounding the wound increases from the mean line tension, $\bar{\Lambda}_0$, to $\bar{\Lambda}_{ps}$, the purse-string tension. The resulting effect is a rapid expansion of wound area after ablation, followed by a contraction back to the original size over 10 minutes. We simulate the tissue dynamics for 300 minutes, or until the wound closes.

**Model implementation**

The model is implemented using Surface Evolver[10]. 200 cells are generated using a Voronoi tessellation and relaxed, without fluctuations and divisions, to a steady state. The simulation is then run, with divisions and fluctuating line tensions, until the tissue has grown to 250 cells. Next, the wound is ablated, and the simulation is run until wound closure or for a maximum of 300 minutes.

**Model parameters**

We use the same normalized contractility $\bar{\Gamma}$ as in Farhadifar *et al.*[8]. Due to differences between our models, such as division rules, the same set of parameters do not apply. The mean division rate is taken from experimental measurements. The wound radius is chosen to ablate the same number of cells as in experiments, and the mean cell area is approximately the cell area measured in experiments. We use the same tension recovery time for line tension $\tau_m$ as in Curran *et al.*[9]. The line tension deviation $\sigma_m$, normalized cell tension $\bar{\Lambda}_0$, and normalized purse-string tension $\bar{\Lambda}_{ps}$, and friction coefficient $\mu$ are chosen to approximate the WT wounded and unwounded intercalation rates, and wound closure time in experiments, and to capture the slow and fast phases of closure.

| Parameter | Symbol | Value |
|---|---|---|
| Normalized contractility | $\bar{\Gamma}$ | 0.04 |
| Normalized cell line tension | $\bar{\Lambda}_0$ | 0.00 |
| Normalized purse string tension | $\bar{\Lambda}_{ps}$ | 0.08 |
| Preferred cell area | $A^0$ | 16 $\mu m^2$ |
| Friction coefficient | $\mu$ | 30 s |
| Cell line tension deviation | $\sigma_m$ | 0.025 |
| Tension recovery time | $\tau_m$ | 150 s |
| Wound radius | $R_w$ | 5.33 $\mu m$ |
| Time step | $\Delta t$ | 3 s |
| Intercalation threshold length | $L_{T1}$ | 0.2 $\mu m$ |
| Mean % Cells Dividing / Hour | | 2.25 |

**Table 2. Default parameters used**

**Computing tissue elastic modulus and viscosity**

We compute tissue shear modulus and viscosity by performing shear rheology simulations on a model tissue comprised of 400 cells. The tissue is sheared in one time step by a strain $\epsilon$, moving each interior vertex position as $x \to x + \epsilon y$. With the boundary vertices held fixed, the sheared tissue is then relaxed for a period of 300 minutes (Supplementary Fig. 5a). During shearing, the strain energy density of the tissue, $E/A$, increases, and then relaxes to a non-zero finite value at long times

(Supplementary Fig. 5b). We obtain the viscoelastic relaxation timescale, $\tau$, and the final strain energy density, $w_\infty$, by fitting an exponential function to the computed strain energy density (Supplementary Fig. 5c).

We run shear rheology simulations for $\epsilon$ in the range 0-0.5 (in steps of 0.025). We compute the shear modulus, $G$, by fitting the equation $w_\infty = w_0 + \frac{1}{2}G\epsilon^2$ (Supplementary Fig. 5d). Due to the fluctuations in energy density from tension fluctuations, the estimate for $\tau$ can be noisy. We obtain an estimate for the average viscoelastic timescale by taking the inverse-variance weighted average of $\tau$ over all values of shear strain: $\bar{\tau} = \frac{\sum_i \tau_i/\sigma_i^2}{\sum_i 1/\sigma_i^2}$. Finally, we obtain the tissue viscosity using the relation, $\eta = G\,\bar{\tau}$.

We verify our calculations by studying the influence of the shape index, $p_0 = -\frac{\Lambda_0}{2\Gamma}$ [11], on the continuum materials properties of the tissue. The shape index has been shown to control a fluid to solid jamming transition, with tissues displaying properties of solids when the shape index is below a critical shape index, $p_0^* \approx 3.81$, and properties of a fluid when above it. We find that as $p_0$ increases the tissue fluidizes, with both the shear modulus and the viscosity decreasing to 0 for $p_0 > 3.8$ (Supplementary Fig. 5e-f). Moreover, we observe a bilinear decrease in the elastic modulus and viscosity, with an initial fast decrease for $p_0 < p_0^*$, and then a slower decrease for $p_0 > p_0^*$, where the shear modulus and viscosity is close to zero.

**Comparing model predictions to experimental perturbations**

To compare the model predictions to the WT wing disc, *Mbs* RNAi, and *Rok* RNAi mutants, we fit the vertex model parameters using the experimentally measured division rates, and the vertex recoil velocities from laser ablation experiments (Fig. 5g). We assume that the recoil velocity is proportional to the effective junctional tension on each cell.

The effective tension is given by $\bar{\Lambda}^{eff} = \frac{1}{2}\bar{\Lambda}_0 + \bar{\Gamma}P^*$, and represents the average tension acting on each cell edge at the junction, where $P^*$ is the cell perimeter that minimizes the tissue mechanical energy. A factor of half is used as each cell edge contributes to half of the total junction tension. Similarly, the effective purse-string tension is given by $\bar{\Lambda}_{ps}^{eff} = \bar{\Lambda}_{ps} + \bar{\Gamma}P^*$, as only one cell contributes to the line tension term.

For WT, *Rok* RNAi, and *Mbs* RNAi tissues, we assume that both the effective tension and the effective purse-string tension are proportional to the initial vertex recoil velocity from laser ablations experiments (Fig. 5g):
$\bar{\Lambda}^{eff} = \beta v$, and $\bar{\Lambda}_{ps}^{eff} = \beta v_{ps}$,
where $\beta$ is the scaling factor, $v$ is the mean tissue edge recoil velocity, and $v_{ps}$ is the mean wound edge recoil velocity from experiments. We use the line tension deviation parameter as before, as this reproduces the unwounded intercalation rate measured experimentally.
We treat both the scaling factor, $\beta$, and the friction coefficient, $\mu$, as our fitting parameters, using the same values in all three cases, to approximate the wound healing rates. From the scaling factor, we obtain the cell junction line tension, and

purse-string tension. The parameters used, that differ from the defaults, are given in Table 3.

| Parameter | *Rok* RNAi Value | WT Value | *Mbs* RNAi Value |
|---|---|---|---|
| $\bar{\Lambda}_0$ | -0.141 | 0.012 | 0.119 |
| $\bar{\Lambda}_{ps}$ | 0.047 | 0.150 | 0.096 |
| $\mu$ | 80s | 80s | 80s |
| Mean % Cells Dividing / Hour | 2.240 | 2.274 | 0.8723 |

**Table 3. Model parameters used in Fig. 5h**

**Live imaging of embryos**

Adult *yw*; Ecad-tdTomato flies were placed in laying cages sealed by agar plates (water 70% v/v, apple juice 30% v/v, agar (Sigma) 3% w/v, methylparaben (Sigma) 0.05% w/v) coated by a small amount of yeast overnight at 25˚C. Embryos were recovered by rinsing the agar plates with water into a basket. Embryos were dechorionated for ~1 minute in 12% sodium hypochlorite solution and rinsed thoroughly with water. Embryos were returned to agar to prevent desiccation and stage 13/14 embryos were selected by eye. Stage 13/14 embryos were affixed to coverslips using heptane glue, with their ventrolateral sides facing the coverslip. Coverslips were then attached to metal slide frames (Leica) using double sided tape and embryos were covered in halocarbon oil 27 (Sigma). Embryos were wounded as above and imaged the same as wing discs, except that 2 minute time intervals were used after the first 25 time points had been acquired. Embryos were allowed to develop to hatching after imaging, to confirm that the imaging process had not been phototoxic. Segmentation of cells was performed as described above.

**Comparing intercalation in embryos and wing discs**

As a measure of how much wound edge intercalation had occurred during embryonic and wing disc wound closure, the percentage of cells remaining close to the centre of the wound was quantified. A circle 5% the area of the original wound was drawn where the centre of the wound was immediately prior to closure. Any cell that intersected this circle immediately after wound closure was scored as having not intercalated away from the wound. The number of cells was then expressed as a percentage of the total number of starting wound edge cells.

**Single junction ablations**

Nanoablation of single junctions was performed to provide a measure of junctional tension[8]. Wing discs were mounted as for wounding experiments and imaged using the same microscope. Narrow rectangular ROIs were drawn across the centre of single junctions and this region was ablated using the same settings used to wound wing discs (see above). Wing discs were imaged continuously in a single plane using identical settings as described above, except that at least 10x zoom was used. The initial recoil rate of vertices at the ends of ablated junctions was quantified by measuring the change in distance between the vertices and dividing by the initial time step. In unwounded discs, no more than two separate junction ablations were performed in each disc, a large distance apart. Ablations in wound edge junctions

were performed 15 minutes after wounding, which corresponded to the time at which myosin II intensity reached its peak. A single junction was ablated in each wound edge.

**Statistical Information**

The results of all statistical test are thoroughly reported in figure legends. Appropriate statistical tests were chosen based on data distributions. Kolmogorov-Smirnov and *t*-tests were two-tailed. For biological experiments, replicates represent wing imaginal discs from different animals. Because the segmentation and tracking process is extremely labour intensive, for each genetic condition 5 replicates were used. This was deemed sufficient, as clear statistical differences could be observed between genotypes. 12 replicate vertex model simulations were run for each parameter set.

**Data Availability Statement**

The data that support the findings of this study are available from the corresponding author upon reasonable request.

**References**


1 Huang, J., Zhou, W. K., Dong, W., Watson, A. M. & Hong, Y. Directed, efficient, and versatile modifications of the Drosophila genome by genomic engineering. *P Natl Acad Sci USA* **106**, 8284-8289, doi:10.1073/pnas.0900641106 (2009).

2 Martin, A. C., Kaschube, M. & Wieschaus, E. F. Pulsed contractions of an actin-myosin network drive apical constriction. *Nature* **457**, 495-U411, doi:10.1038/nature07522 (2009).

3 Royou, A., Field, C., Sisson, J. C., Sullivan, W. & Karess, R. Reassessing the role and dynamics of nonmuscle myosin II during furrow formation in early Drosophila embryos. *Mol Biol Cell* **15**, 838-850, doi:10.1091/mbc.E03-06-0440 (2004).

4 Jordan, P. & Karess, R. Myosin light chain-activating phosphorylation sites are required for oogenesis in Drosophila. *Journal of Cell Biology* **139**, 1805-1819, doi:DOI 10.1083/jcb.139.7.1805 (1997).

5 Oda, H. & Tsukita, S. Real-time imaging of cell-cell adherens junctions reveals that Drosophila mesoderm invagination begins with two phases of apical constriction of cells. *J Cell Sci* **114**, 493-501 (2001).

6 Zartman, J., Restrepo, S. & Basler, K. A high-throughput template for optimizing Drosophila organ culture with response-surface methods (vol 140, pg 667, 2013). *Development* **140**, 2848-2848, doi:10.1242/dev.098921 (2013).

7 Heller, D. *et al.* EpiTools: An Open-Source Image Analysis Toolkit for Quantifying Epithelial Growth Dynamics. *Dev Cell* **36**, 103-116, doi:10.1016/j.devcel.2015.12.012 (2016).

8 Farhadifar, R., Roper, J. C., Algouy, B., Eaton, S. & Julicher, F. The influence of cell mechanics, cell-cell interactions, and proliferation on epithelial packing. *Current Biology* **17**, 2095-2104, doi:10.1016/j.cub.2007.11.049 (2007).

9 Curran, S. *et al.* Myosin II Controls Junction Fluctuations to Guide Epithelial Tissue Ordering. *Dev Cell* **43**, 480-492 e486, doi:10.1016/j.devcel.2017.09.018 (2017).

10 Brakke, K. A. The Surface Evolver. *Experimental Mathematics* **1**, 141-165, doi:10.1080/10586458.1992.10504253 (1992).
11 Bi, D. P., Lopez, J. H., Schwarz, J. M. & Manning, M. L. A density-independent rigidity transition in biological tissues. *Nat Phys* **11**, 1074-+, doi:10.1038/Nphys3471 (2015).

## Supplementary Figures

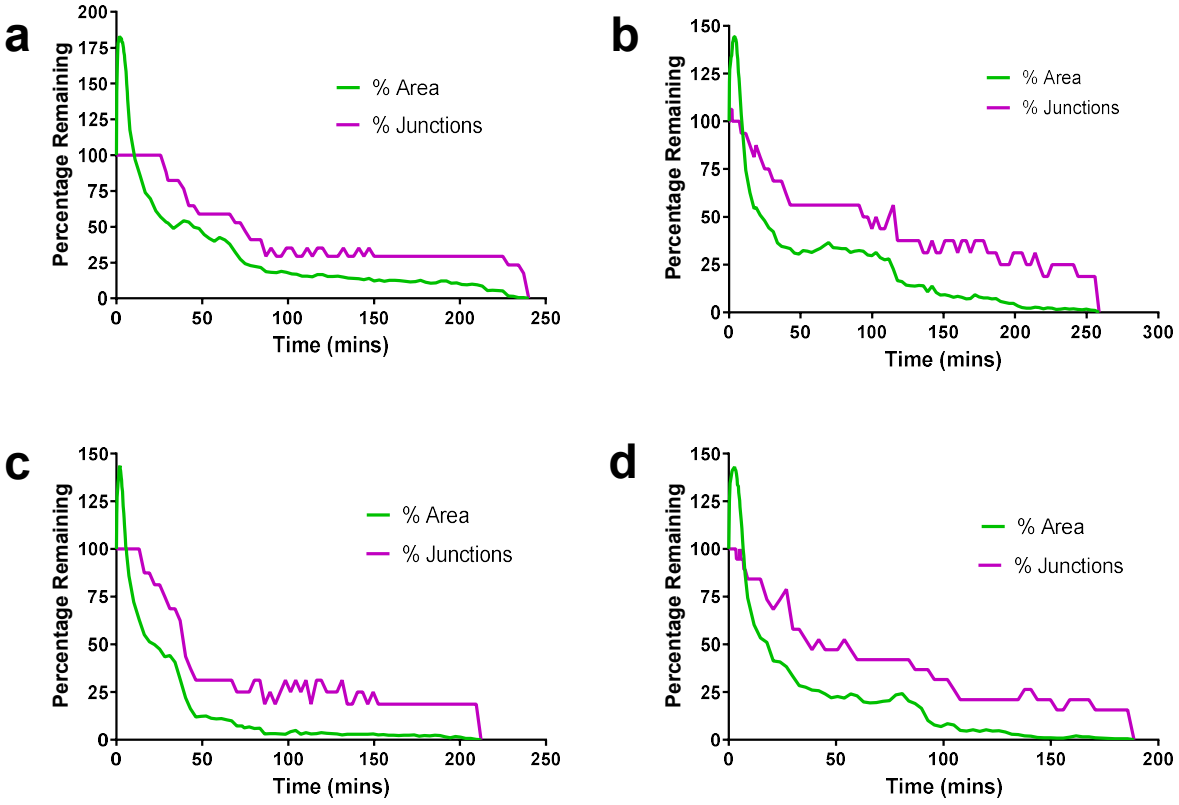


**Supplementary Figure 1. Relationship between wound area changes and intercalation events in WT wing discs**

**a-d,** Quantification of the percentage of starting wound edge junctions (magenta) and wound percentage area (green) for four Ecad-GFP wing disc wounds (in addition to the wing disc in Fig. 1e).

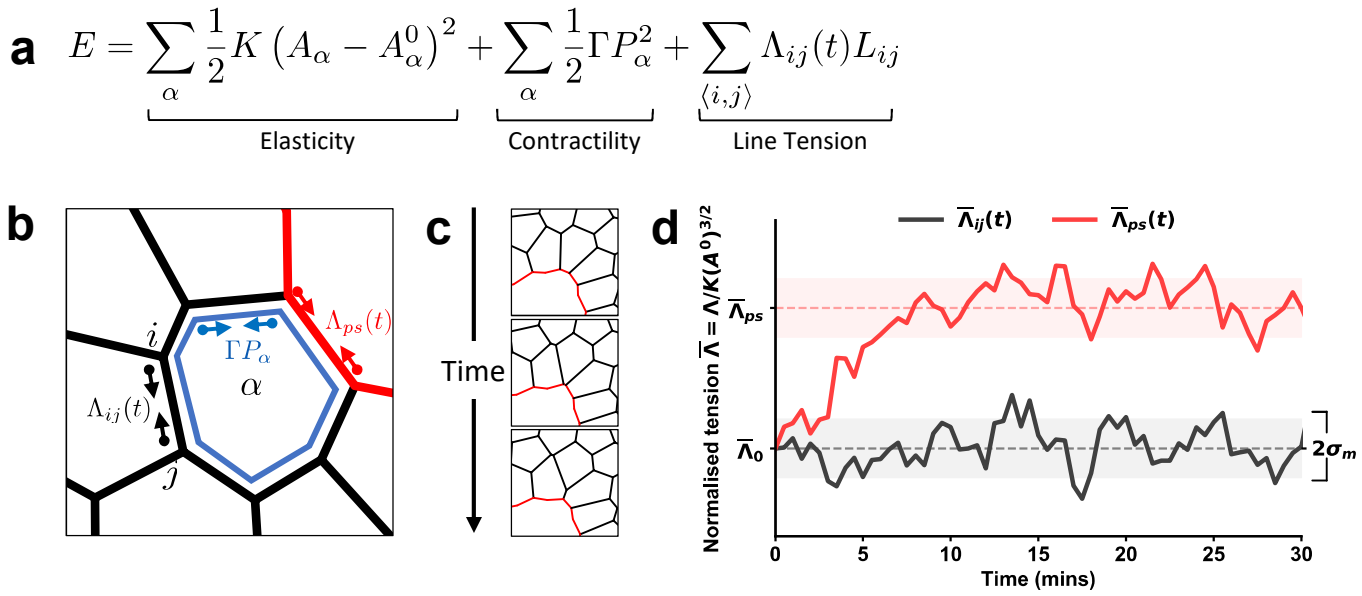


**Supplementary Figure 2. Vertex modelling of wound healing**

**a**, Equation for the total energy of the system. **b**, Schematic showing the forces due to line tension and contractility acting on a cell in the vertex model. **c**, Example of a wound edge intercalation. **d,** Cell edge line tension fluctuation (black) and purse-string tension on the wound (red) over time after ablation (T = 0 mins).

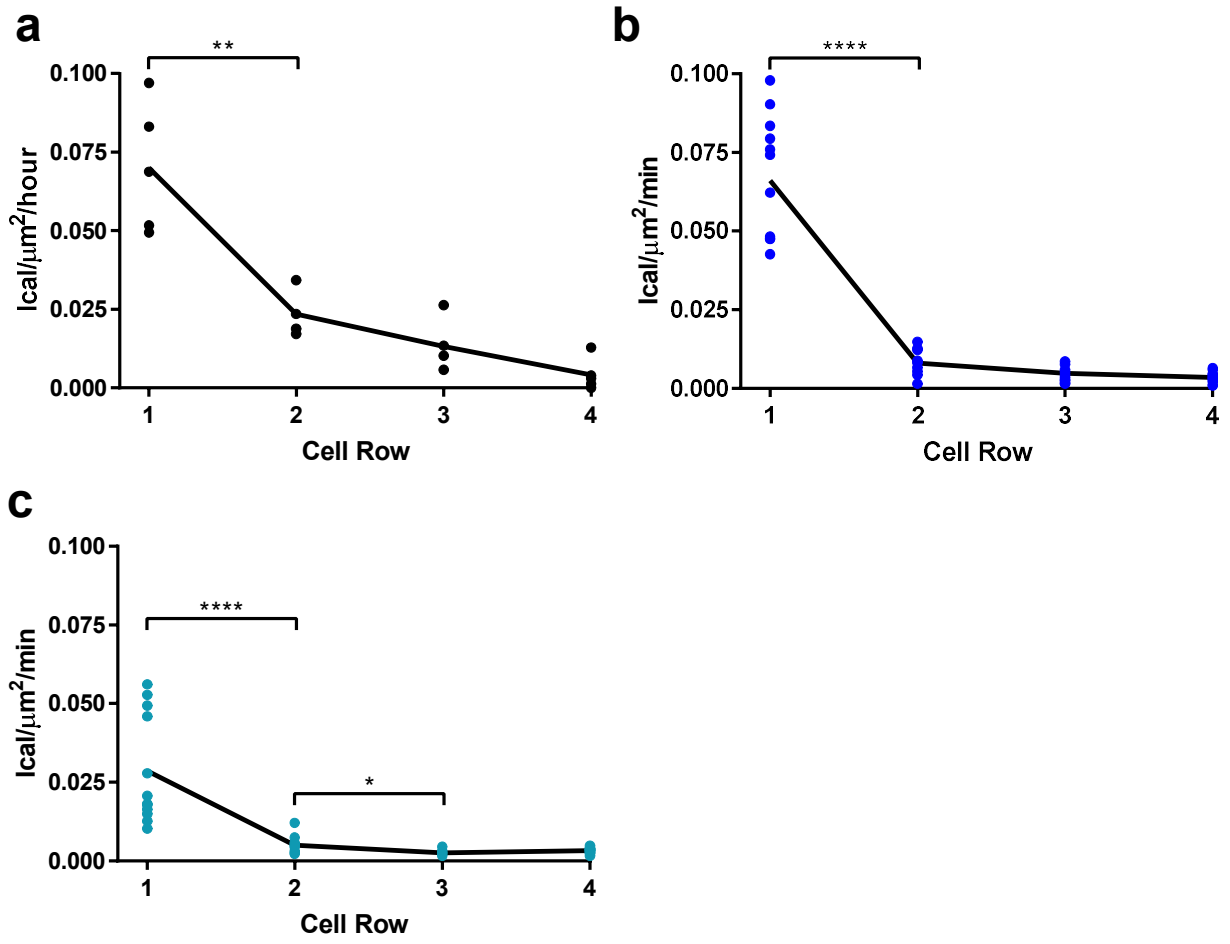


**Supplementary Figure 3. Analysis of intercalation rate in rows of cells away from the wound**

**a-c**, Intercalation rates expressed as the number of intercalations per μm$^2$ per min for (**a**) WT wing discs and vertex model simulations with (**b**) high or (**c**) low purse string tensions in rows of cells away from the wound edge. Statistically significant differences between neighbouring rows are shown. The intercalation rate was significantly higher in row 1 than row 2 for WT wing discs (Kolomogorov-Smirnov Test, D=1, $p$=0.0079), high purse string (Kolomogorov-Smirnov Test, D=1, $p$<0.0001) and low purse string (Kolomogorov-Smirnov Test, D=0.9167, $p$<0.0001) simulations. In low purse string simulations, the intercalation rate was also significantly higher in row 2 than row 3 (Kolomogorov-Smirnov Test, D=0.5833, $p$=0.0337).

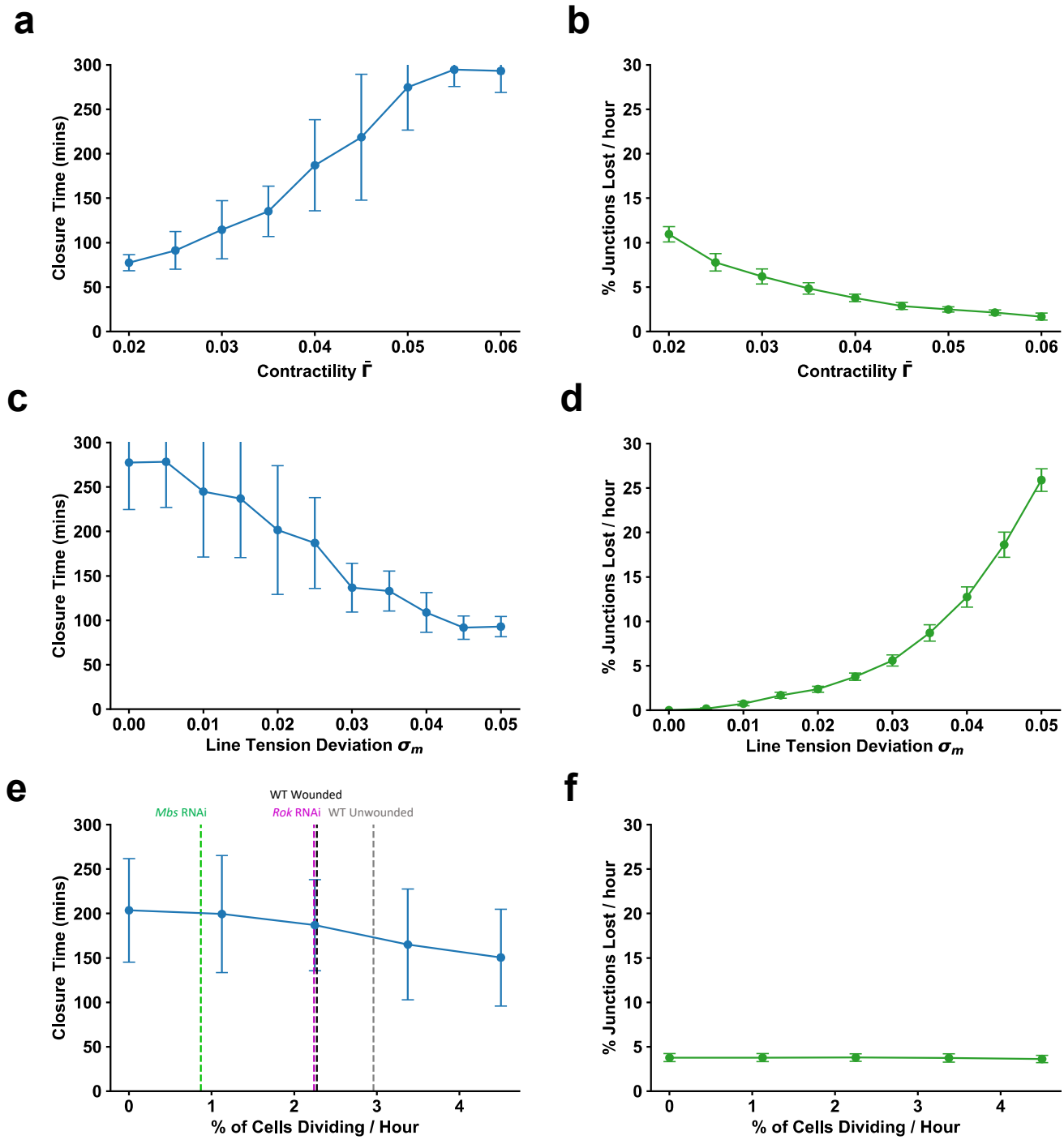


**Supplementary Figure 4. Effect of model parameters on fluidity and closure time**

**a**, Mean intercalation rate in a wounded tissue, and **b**, mean closure time against normalized contractility. **c**, Mean intercalation rate in a wounded tissue, and **d**, mean closure time against cell line tension deviation. **e**, Mean intercalation rate in a wounded tissue, and **f**, mean closure time against cell division rate. For each value, (n = 12). Dashed lines indicate experimentally measured values of division rates.

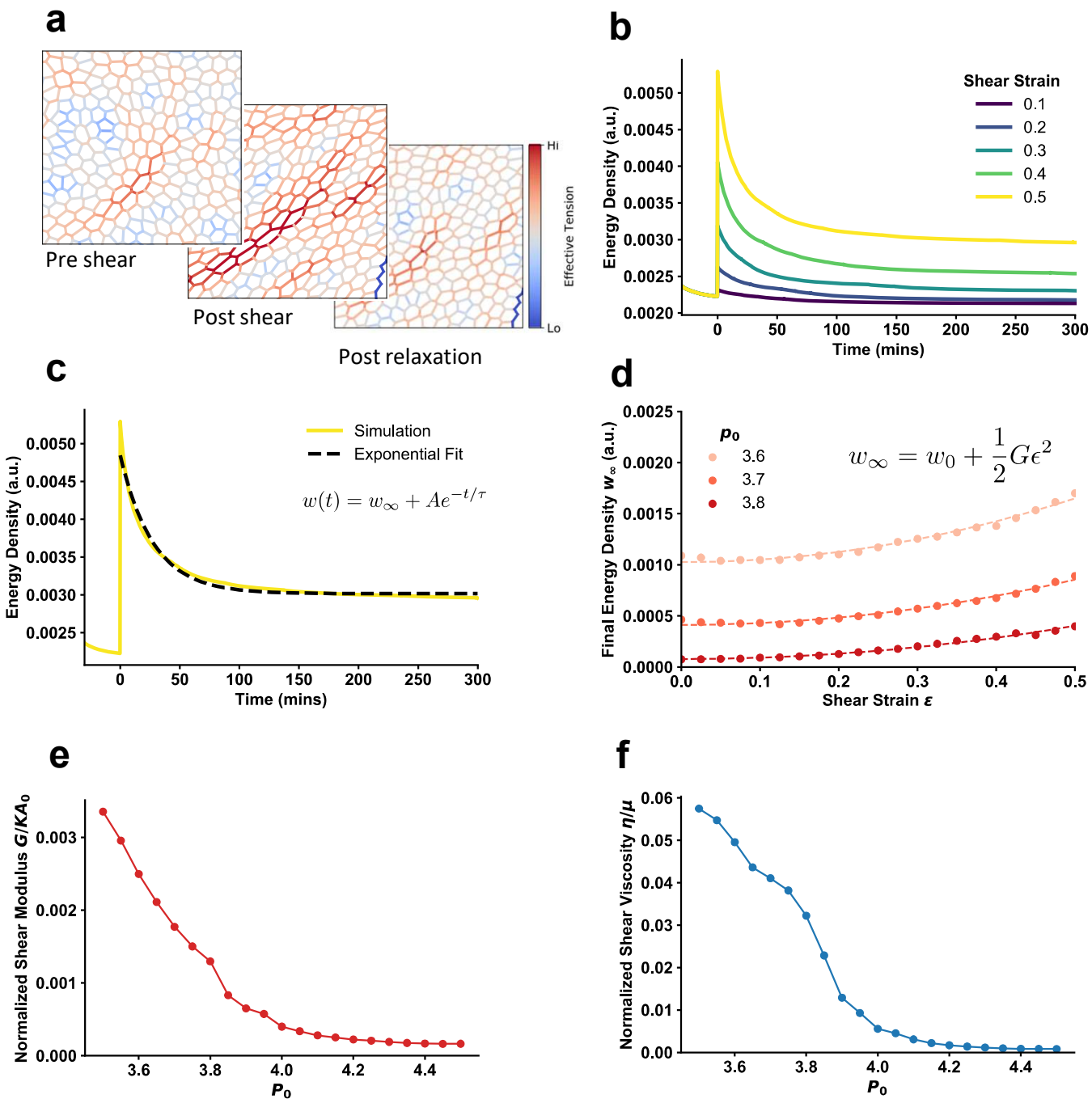
a
Pre shear
Post shear
Post relaxation
Hi
Lo
Effective Tension
b
Shear Strain
0.1
0.2
0.3
0.4
0.5
Energy Density (a.u.)
Time (mins)
c
Simulation
Exponential Fit
$w(t) = w_\infty + Ae^{-t/\tau}$
Energy Density (a.u.)
Time (mins)
d
$p_0$
3.6
3.7
3.8
$w_\infty = w_0 + \frac{1}{2}G\epsilon^2$
Final Energy Density $w_\infty$ (a.u.)
Shear Strain $\epsilon$
e
Normalized Shear Modulus $G/KA_0$
$P_0$
f
Normalized Shear Viscosity $\eta/\mu$
$P_0$

**Supplementary Figure 5. Obtaining continuum tissue properties by shearing**

**a,** Images of a tissue during shearing simulations, before shearing, after shearing, and after relaxation. Edge color indicates the effective tension, the total of the line tension and contractility, on each edge, with blue being low and red high. **b**, The energy density of the tissue over time, for different amounts of shear strain. **c**, An exponential curve is fit to the energy density, giving a relaxation time scale, $\tau$, and a final strain energy, $w_\infty$. **d**, Final energy density, $w_\infty$, against shear strain, for different values of $p_0$. The shear strain is obtained by fitting a quadratic curve. **e**, The normalized tissue shear modulus against cell shape index $p_0$. **f**, The normalized tissue viscosity against cell shape index $p_0$.

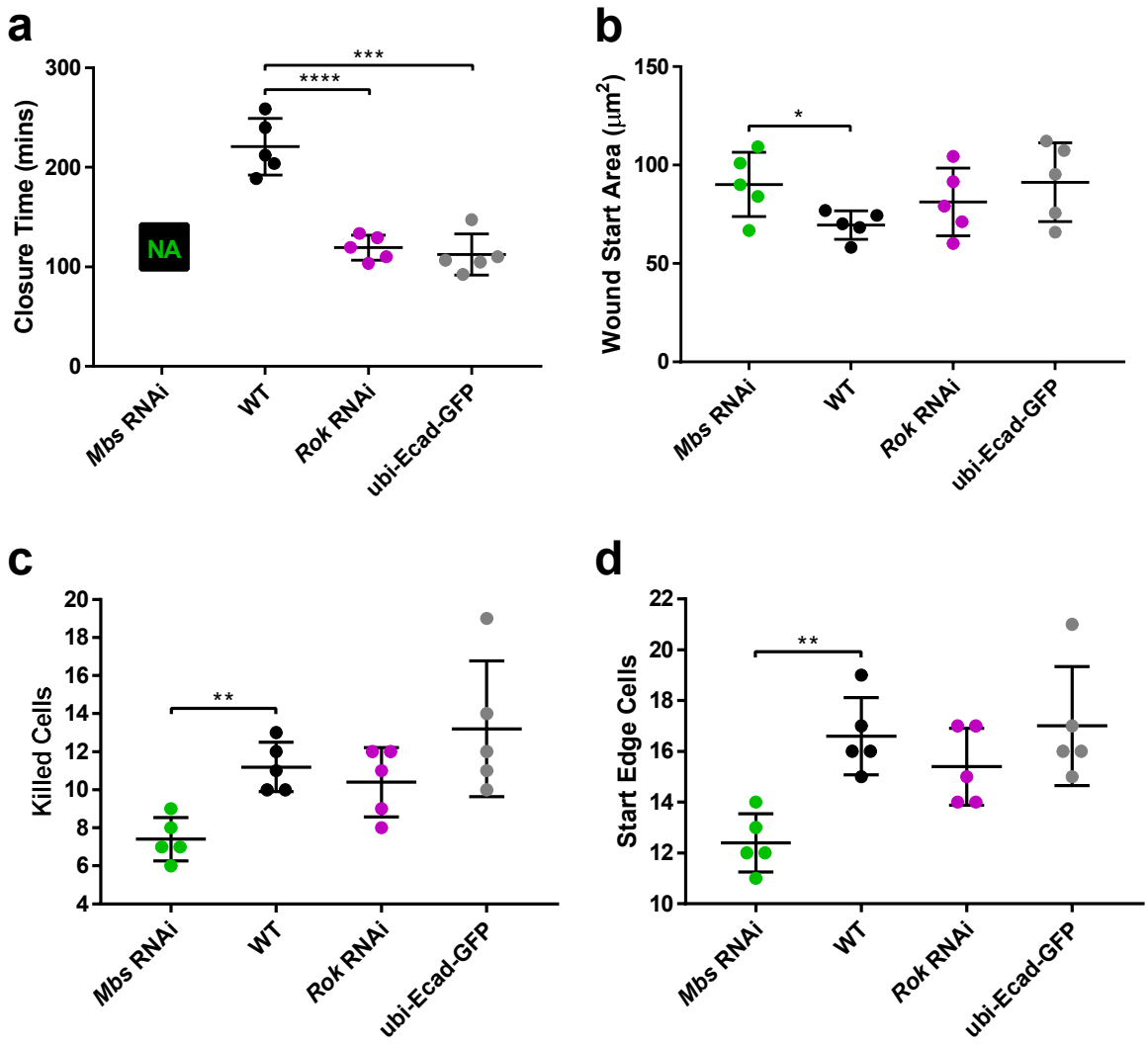


**Supplementary Figure 6. Comparisons of features of *Mbs* RNAi, *Rok* RNAi, ubi-Ecad-GFP and WT wounds**

**a,** Quantification of time of closure. *Rok* RNAi (unpaired *t*-test, $t$=7.318, $df$=8, $p$<0.0001) and ubi-Ecad-GFP (unpaired *t*-test, $t$=6.907, $df$=8, $p$=0.0001) wounds close in less time than WT wounds. *Mbs* RNAi wounds fail to close. **b,** Quantification of wound start areas. WT wounds were smaller than *Mbs* RNAi wounds (unpaired *t*-test, $t$=2.585, $df$=8, $p$=0.0324). **c,** Quantification of number of cells killed. Fewer cells were killed in *Mbs* RNAi wounds than in WT (unpaired *t*-test, $t$=4.906, $df$=8, $p$=0.0012). **d,** Quantification of starting wound edge cells. *Mbs* RNAi wounds had fewer starting edge cells than WT (unpaired *t*-test, $t$=4.95, $df$=8, $p$=0.0011). **a-d,** Error bars = SD. All statistical tests were performed against WT and were only reported if significant.

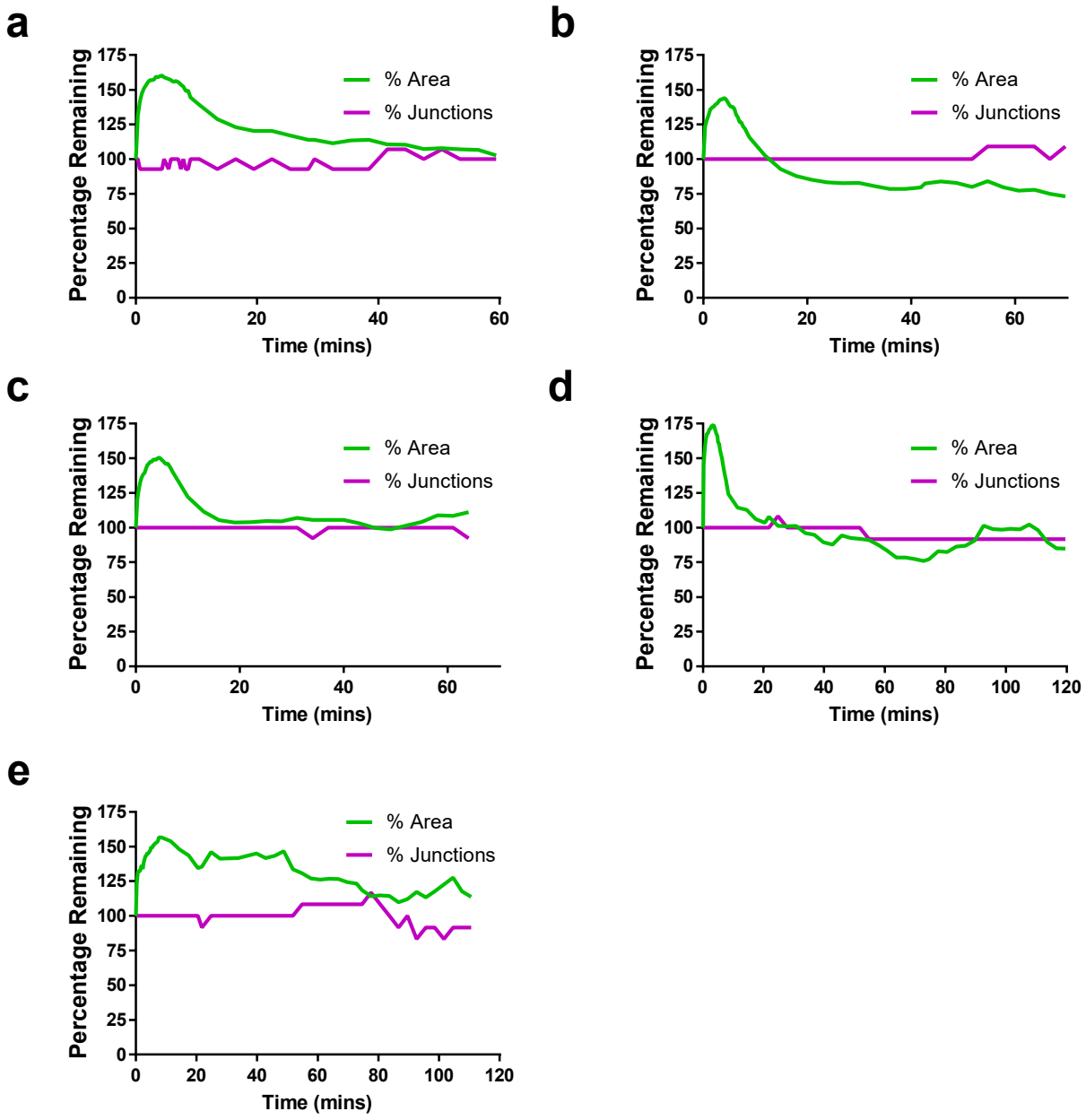


**Supplementary Figure 7. Relationship between wound area changes and intercalation events in *Mbs* RNAi wing discs**

**a-e,** Quantification of the percentage of starting wound edge junctions (magenta) and wound percentage area (green) for five Ecad-GFP/UAS-*Mbs*-RNAi; *rn*-GAL4/+ wing disc wounds.

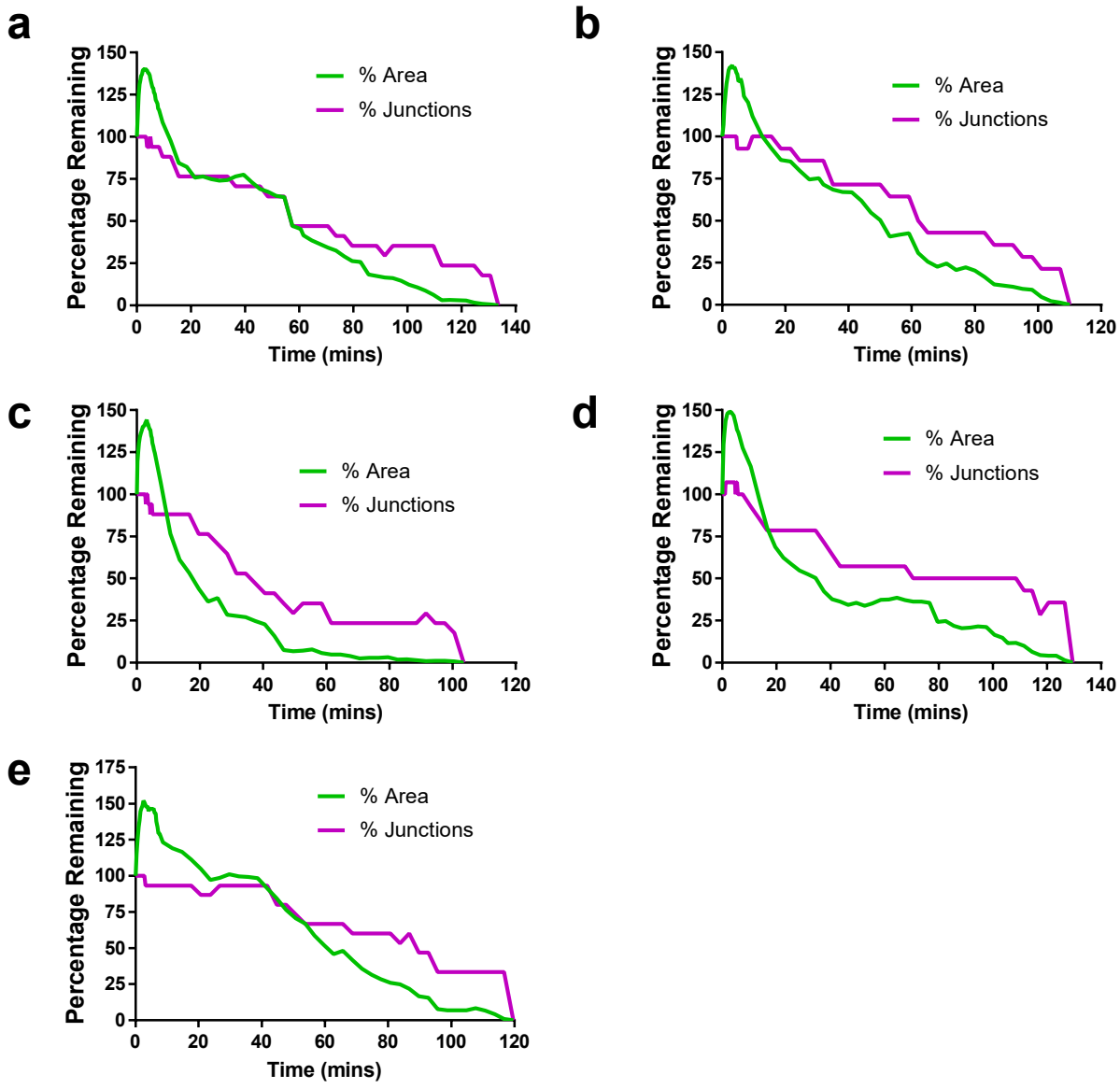


**Supplementary Figure 8. Relationship between wound area changes and intercalation events in *Rok* RNAi wing discs**

**a-e,** Quantification of the percentage of starting wound edge junctions (magenta) and wound percentage area (green) for five Ecad-GFP/UAS-*Rok*-RNAi; *rn*-GAL4/+ wing disc wounds.

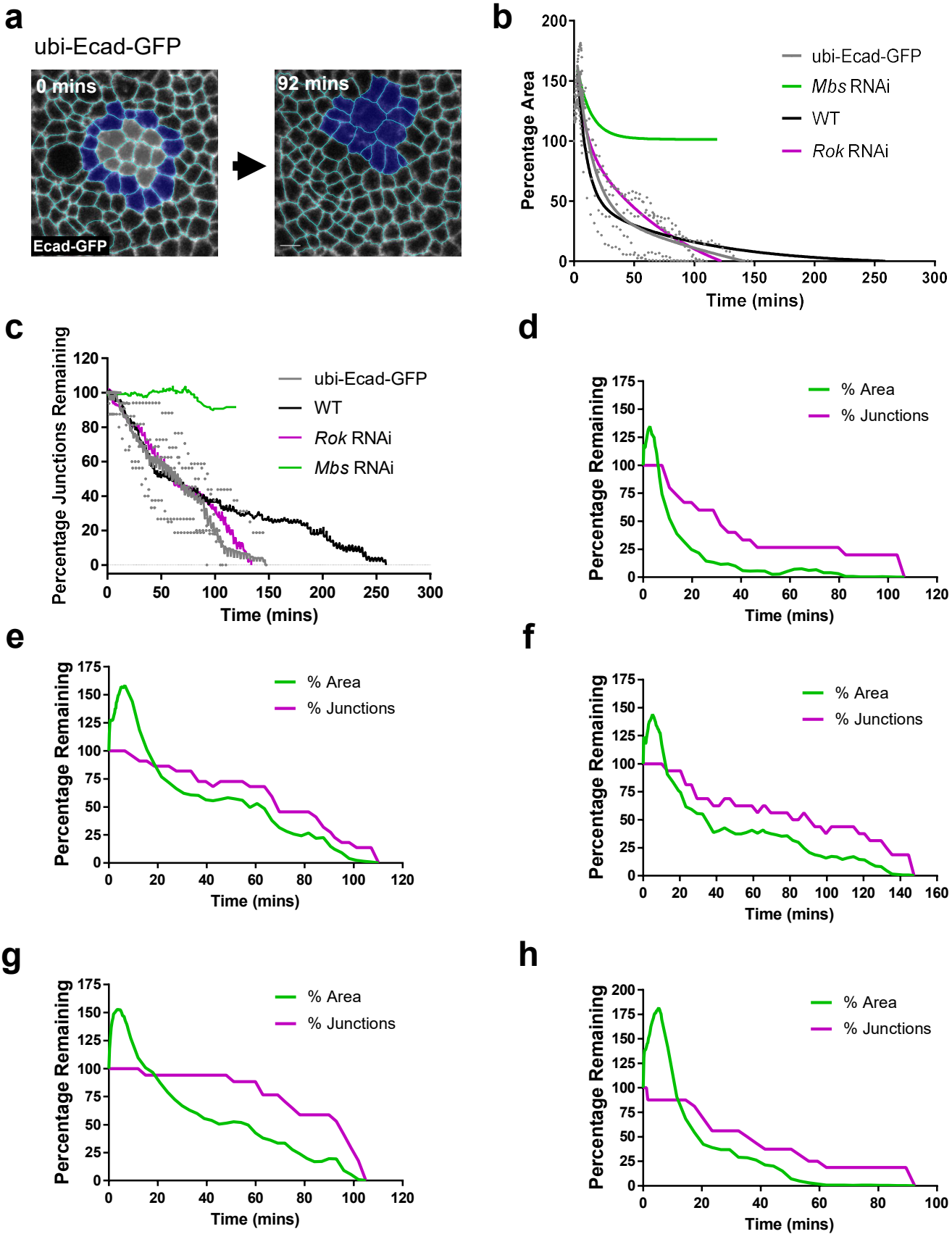
a
ubi-Ecad-GFP
0 mins
92 mins
Ecad-GFP
b
Percentage Area
Time (mins)
ubi-Ecad-GFP
Mbs RNAi
WT
Rok RNAi
c
Percentage Junctions Remaining
Time (mins)
ubi-Ecad-GFP
WT
Rok RNAi
Mbs RNAi
d
Percentage Remaining
Time (mins)
% Area
% Junctions
e
Percentage Remaining
Time (mins)
% Area
% Junctions
f
Percentage Remaining
Time (mins)
% Area
% Junctions
g
Percentage Remaining
Time (mins)
% Area
% Junctions
h
Percentage Remaining
Time (mins)
% Area
% Junctions

**Supplementary Figure 9. Wound closure dynamics in ubi-Ecad-GFP wing discs.**

**a,** Example of wound healing in a ubi-Ecad-GFP wing disc before wounding (left) and after wound closure (right). Starting wound edge cells are marked in dark blue. Images are adaptive projections of Ecad-GFP overlaid by skeletonised cell outlines in cyan (scale bar = 3μm). **b,** Quantification of wound closure (as percentage of start wound area) over time in ubi-Ecad-GFP wing discs (grey, n=5) with a two-phase exponential decay fitted after 3 minutes. ubi-Ecad-GFP data is overlaid on two-phase exponential decays (from Fig. 5b) for WT (black), *Rok* RNAi (magenta) and *Mbs* RNAi (green). **c,** Quantification of the percentage of initial wound edge junctions over time for ubi-Ecad-GFP wing discs (colours and n numbers as in b) with a moving average curve ($\pm$4 time points) shown. Data is overlaid on moving average curves (from Fig. 5e) for WT, *Rok* RNAi and *Mbs* RNAi. **d-h**, Quantification of the percentage of starting wound edge junctions (magenta) and wound percentage area (green) for five ubi-Ecad-GFP wing disc wounds.

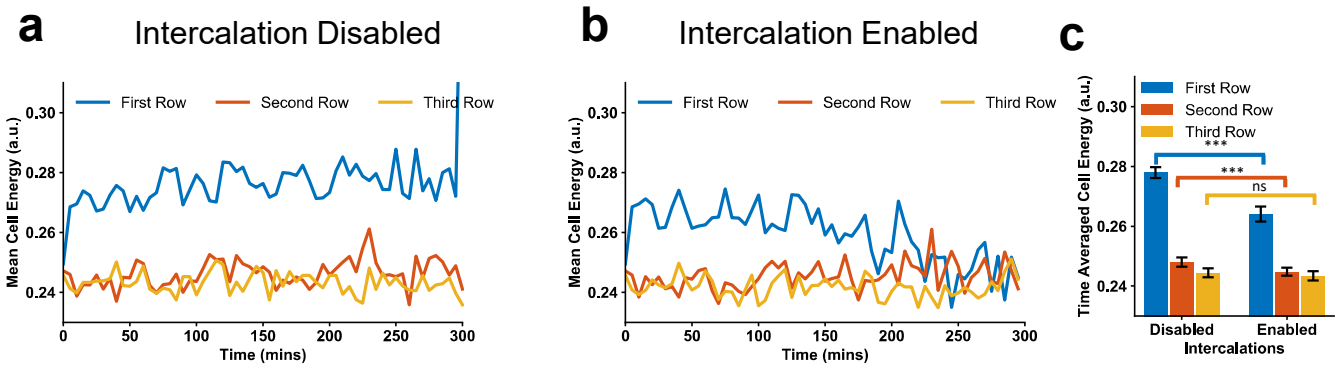


**Supplementary Figure 10. Effect of intercalations on cell energy**

**a-b,** Mean cell mechanical energy over time for the first three rows of cells with intercalations (**a)** enabled, and (**b)** disabled. **c,** Quantification of time averaged cell energy for the first three rows, with intercalations enabled and disabled, averaged over 12 simulations. With intercalations enabled, the mean cell area is lower in the first row (unpaired *t*-test, *t*=14.8, *df*=22, *p*<1e-12), second row (unpaired *t*-test, *t*=5.282, *df*=22, *p*<1e-4), and third row (unpaired *t*-test, *t*=1.642, *df*=22, *p*>1e-1). Error bars = SD.

| | *Rok* RNAi Tissue | *Rok* RNAi Wound | WT Tissue | WT Wound | *Mbs* RNAi Tissue | *Mbs* RNAi Wound |
|---|---|---|---|---|---|---|
| *Rok* RNAi Tissue | | <0.0001 (0.8078) | 0.002 (0.5845) | <0.0001 (0.95) | <0.0001 (0.913) | <0.0001 (0.8604) |
| *Rok* RNAi Wound | | | 0.0167 (0.5088) | 0.0019 (0.5974) | 0.9368 (0.1974) | 0.1516 (0.3684) |
| WT Tissue | | | | 0.0002 (0.6889) | 0.0033 (0.6667) | 0.0019 (0.614) |
| WT Wound | | | | | 0.0365 (0.5167) | 0.2506 (0.3263) |
| *Mbs* RNAi Tissue | | | | | | 0.6884 (0.2632) |
| *Mbs* RNAi Wound | | | | | | |

**Supplementary Table 1. Results of Kolmogorov Smirnov tests comparing vertex recoil rates in *Rok* RNAi, WT and *Mbs* RNAi wing discs**

Results of Kolmogorov Smirnov tests for pairwise comparisons of all combinations of vertex recoil rates at the wound edge and in the surrounding tissue in *Rok* RNAi, WT and *Mbs* RNAi wing discs. *p* values and the Kolomogorov Smirnov D statistic (in brackets) are shown. Statistically significant comparisons are highlighted in green.

## Supplementary Video Legends

**Supplementary Video 1. Myosin II localisation during *Drosophila* wing disc wound closure.** Time-lapse of the first hour after wounding in a $sqh^{AX3}$; *sqh*-GFP, Ecad-tdTomato wing imaginal disc. Myosin II is marked by Sqh-GFP (magenta, maximum intensity projection) and cell outlines by Ecad-tdTomato (green, adaptive projection). Myosin II rapidly accumulates at the wound's edge in the manner of a purse string.

**Supplementary Video 2. WT wound closure.** Time-lapse of an Ecad-GFP/+; *rn*-GAL4/+ (WT) wing disc from wounding to wound closure. An adaptive projection of Ecad-GFP (greyscale) is overlaid with skeletonised cell outlines (cyan). The wound itself (white) and initial wound edge cells (blue) are highlighted.

**Supplementary Video 3. Vertex model simulation of wound healing with intercalations disabled.** Red edges represent the wound edge and have increased line tension compared to the surrounding tissue (black edges). The wound fails to close during the simulation.

**Supplementary Video 4. Vertex model simulation of wound healing with intercalations enabled.** The same parameters are used as in Supplementary Video 3, except that intercalations are enabled. The wound is able to close.

**Supplementary Video 5. Analysing the first three rows of cells away from the wound.** Time-lapse of an Ecad-GFP/+; *rn*-GAL4/+ (WT) wing disc from wounding to wound closure. An adaptive projection of Ecad-GFP (greyscale) is overlaid with skeletonised cell outlines (cyan). The wound itself is highlighted in white. The first (blue), second (orange) and third (yellow) rows of cells away from the wound are selected prior to wounding. These initial cell identities are propagated through time, regardless of whether the cell intercalates or not.

**Supplementary Video 6. Wound closure in an *Mbs* RNAi wing disc.** Time-lapse of an Ecad-GFP/UAS-*Mbs*-RNAi; *rn*-GAL4/+ wing disc after wounding. The wound fails to close during imaging. An adaptive projection of Ecad-GFP (greyscale) is overlaid with skeletonised cell outlines (cyan). The wound itself (white) and initial wound edge cells that do intercalate (blue) and do not intercalate (cyan) are highlighted.

**Supplementary Video 7. Wound closure in a *Rok* RNAi wing disc.** Time-lapse of an Ecad-GFP/UAS-*Rok*-RNAi; *rn*-GAL4/+ wing disc from wounding to wound closure. An adaptive projection of Ecad-GFP (greyscale) is overlaid with

skeletonised cell outlines (cyan). The wound itself (white) and initial wound edge cells (blue) are highlighted.